Nanoscale

PAPER

View Article Online
View Journal | View Issue

Cite this: *Nanoscale*, 2025, **17**, 7218

Exploring piezoelectric and piezophototronic properties of nanostructured LN-$ZnSnS_3$ for photoresponsive vibrational energy harvesting†

Surajit Das,‡[a] Swadesh Paul‡[a] and Anuja Datta *[a,b]

Piezoelectric energy harvesters have for some time been an advanced choice for self-powered electronics. While oxide-based piezoelectric nanomaterials are well studied for their quality mechanical energy harvesting potential, recent interest in developing multifunctional nanomaterials for harvesting simultaneous ferroelectric/piezoelectric and light energy for photodetectors, photovoltaics and piezophototronics has impelled the search for newer semiconducting dipolar materials. In this respect, $LiNbO_3$ type-$ZnSnS_3$ (LN-ZTS) is predicted to have low optical band gap energy and to possess a considerably expanded hexagonal *R3c* lattice with high ferroelectricity. Although it has been stabilised in thin-film form, the exclusive synthesis of LN-ZTS nanocrystals has not been reported. In this article, we report a one-step synthesis for *R3c* hexagonal LN-type $ZnSnS_3$ (ZTS) nanoflakes and show that they could be highly desirable candidates for light-responsive mechanical energy harvesting *via* an impressive piezophototronic effect. A piezoelectric coefficient (d_{33}) of ~19 pm V^{-1} was measured using piezoresponse force microscopy and a considerable zero-bias photoconduction current was observed, which was utilized to harvest an output power of ~0.13 μW cm^{-2} from an induced light intensity of 100 mW cm^{-2} under a mechanical impact of 17 N and 3 Hz. These findings establish a previously unreported ternary sulfide piezoelectric nanostructured material as potential candidate for designing piezophototronic devices by coupling optical functionalities and piezoelectric responses.

Received 12th December 2024,
Accepted 14th February 2025

DOI: 10.1039/d4nr05246c

rsc.li/nanoscale

Introduction

Lead-free and nontoxic piezoelectric nanomaterials, due to their sustainable and enhanced abilities to convert mixed-mechanical stimuli into electrical energy, are increasingly becoming a viable choice for self-powered microelectronics applications.[1–3] To search for new materials with emergent piezoelectric and allied physical properties, particularly at nanoscale, where enhanced dipolar density and significantly shorter transport paths of ions and electrons can impart a higher piezoelectric effect, researchers are focusing on designing and engineering different nanostructures of predicted materials and those that have already undergone experimentation, by applying various low-cost fabrication techniques.[4–6] While eco-friendly oxide-based piezoelectric materials have been well studied for their stable piezoelectric properties,[7–10] other chalcogenide compounds are rarely explored. A recently discovered interesting ferroelectric and potentially piezoelectric material, $LiNbO_3$-structured $ZnSnS_3$ (LN-$ZnSnS_3$) is being studied for its suitability, with additional semiconducting properties that open up the possibility of investigating both mechanical and light energy harvesting capabilities by inducing piezophotonic and piezophoto electronic effects simultaneously.[11–14] Here, piezoelectric potential in mid–high band gap semiconductors can be created by photoexcitation and serves as the fundamental principle behind the piezophototronic effect. The piezophototronic effect is observed primarily in non-centrosymmetric semiconductors that exhibit both piezoelectric and optoelectronic properties, such as ZnO, GaN, CdS, and PbS to name a few, and was a benchmark discovery by Z. L. Wang.[1–4] The piezophototronic effect on its own can use piezopotential to influence the energy band gap and optical band gap for the generation, separation, transportation, and recombination of carriers at interfaces. Possessing simultaneous piezoelectric and semiconducting optical properties, this special class of material offer possibilities for designing and fabricating

[a]*School of Applied and Interdisciplinary Sciences, Indian Association for the Cultivation of Science, 2A and 2B Raja S. C. Mullick Road, Kolkata, 700032, India. E-mail: psuad4@iacs.res.in*
[b]*Technical Research Centre, Indian Association for the Cultivation of Science, 2A and 2B Raja S. C. Mullick Road, Kolkata, 700032, India*

†Electronic supplementary information (ESI) available. See DOI: https://doi.org/10.1039/d4nr05246c

‡Equally contributing.

devices with potential applications in self-powdered sensors and devices, nanorobotics, optoelectronics and photonics, and logic computation.[12,15–19] Interest is therefore largely devoted toward exploring newer materials with large internal electric fields and hence ferroelectric/piezoelectric effects that could be simultaneously exploited in junction-less photoelectric and photovoltaic applications,[20–23] as traditional large band gap (3–4 eV) ferroelectrics are unsuitable for efficient light harvesting. In that respect, theoretical findings show that the compound LN-$ZnSnS_3$ formed as a thin film by substituting the oxygen in ferroelectric LN-$ZnSnO_3$ with sulfur, dramatically lowers the optical band gap energy from 3.0 eV (LN-$ZnSnO_3$) to 1.3 eV (LN-$ZnSnS_3$), due to considerable expansion of the lattice parameters (~20%), without compromising the high ferroelectricity reported in LN-$ZnSnO_3$.[24–34] Moreover, it is an added advantage that the band gap reduction in LN-$ZnSnS_3$ does not require strain engineering.[35] This report was followed by the claim that LN-$ZnSnS_3$ is a highly ferroelectric phase in spite of its low band gap and semiconducting nature, which are desirable characteristics for junction-less photovoltaic applications and also as piezophototronic energy harvesters.[36] In an attempt to increase the library of materials among lead-free perovskites and to introduce a novel semiconducting piezo-ferroelectric class of compounds, we recently investigated the synthesis, growth and functional properties of undoped and doped LN-type $ZnSnO_3$ nanostructures, that boosted the importance of application-based research on sustainable ceramic nanomaterials and nanocomposites for harvesting energy.[21,37–41]

Herein, we report the synthesis of R3c LN-type $ZnSnS_3$ (ZTS) nanocrystals (NCs) and show that they can be highly desirable candidates for light-responsive mechanical energy harvesting *via* an impressive piezophototronic effect. In this work, largely phase-pure LN-phase ZTS NCs are synthesized by a facile, optimised one-step hydrothermal method and the fundamental piezoelectric and photoconducting properties are explored under mechanical force. While the synthesis of cubic phase ZTS was reported earlier, a viable low-cost approach towards the synthesis of the much more important rhombohedral phase of LN-ZTS[35,42] could not be found. An average piezoelectric coefficient of ~19 pm V^{-1} is obtained from piezoresponse force microscopy (PFM) measurements, and the domain characteristic envisaged by PFM indicates clear piezoelectric polarisation reversal in LN-ZTS NCs. The material promisingly shows vibrational energy harvesting potential with a peak output voltage of 0.5 V and a power density of 0.025 μW cm^{-2} for optimal conditions of 17 N and 3 Hz, in the absence of added illumination, henceforth referred as "dark" condition. Thus, when stimulated with light, the LN-ZTS nanogenerator (NG) shows an enhanced peak output voltage and five-fold enhanced power density of 0.8 V and 0.13 μW cm^{-2}, respectively, under similar measurement conditions for an incident 100 mW cm^{-2} light intensity. While the power output is still low for direct practical application, evidence of the first piezoelectric and light-induced enhancement in power output from LN-$ZnSnS_3$ at nanoscale, will surely excite the non-oxide-based ceramics community to explore emerging photovoltaic and ferro-functional properties, which were hitherto unexplored territory for this material.

Chemicals and experimental procedure

Chemicals

Zinc chloride ($ZnCl_2$, ≥97%), sodium stannate trihydrate ($Na_2SnO_3{\cdot}3H_2O$, 95%), and reagent-grade sulfur powder (100 mesh) were purchased from Sigma-Aldrich. Thioacetamide (C_2H_5NS, >98%) was obtained from TCI. Absolute ethanol (EtOH) and D.I. H_2O were obtained from Merck. All materials were used without any further purification.

Synthesis of $ZnSnS_3$ (ZTS) nanocrystals (NCs)

A one-step hydrothermal method was exploited for the synthesis of LN-ZTS NCs. In a typical synthesis, 1 mmol of $ZnCl_2$ (136.3 mg), 1 mmol of $Na_2SnO_3{\cdot}3H_2O$ (267 mg), and 3 mmol of C_2H_5NS (226 mg) were dissolved in 36 ml D.I. H_2O and sonicated for 15 min. In the next step the complete mixture solution was stirred with a magnetic stirrer for 3 h. An intermediate white suspension was obtained, which was then transferred to a Teflon-lined stainless steel autoclave and thereafter to a preheated gravity convection oven (Bionics Scientific Technologies Ltd), heated at 220 °C for different times of 6 h, 18 h and 24 h. After completion of the reaction, the autoclave was cooled to room temperature and the products were collected by centrifugation with absolute EtOH several times. Finally, they were dried in a vacuum oven at 70 °C for 6 h. The complete reaction procedure is illustrated in Scheme 1.

Device preparation for piezophototronic measurements

Electrical and photonic measurements were carried out on LN-ZTS pellets prepared from the synthesized powder of LN-ZTS NCs. Hydraulic pressing under 110 kg cm^{-2} pressure generated a pellet of a thickness of 2 mm with a diameter of 10 mm and an average density of 0.191 g cm^{-3}. Gold (Au) electrodes were deposited on both sides of the pellet by employing the chemical vapour deposition (CVD) technique. For the piezophototronic measurements, patterned Au electrodes were chosen for deposition using a shadow mask to leave access for the light to fall on the material surface, while the Au patterned electrodes were suitable for use in the capacitor device structure needed for vibrational energy harvesting.[43]

Characterization details

The phase and crystal structure were investigated using powder X-ray diffraction (PXRD), collected with a Bruker-D8 Advanced X-ray diffractometer with Cu K_α radiation (λ = 1.5406 Å). The chemical composition was determined by X-ray photoelectron spectroscopy (Omicron DAR 400 dual Mg/Al source spectrometer) and energy dispersive X-ray spectroscopy (EDS) under TEM. The reflectance spectra and optical band gap of ZTS NCs were measured with an Agilent Cary 5000, UV–

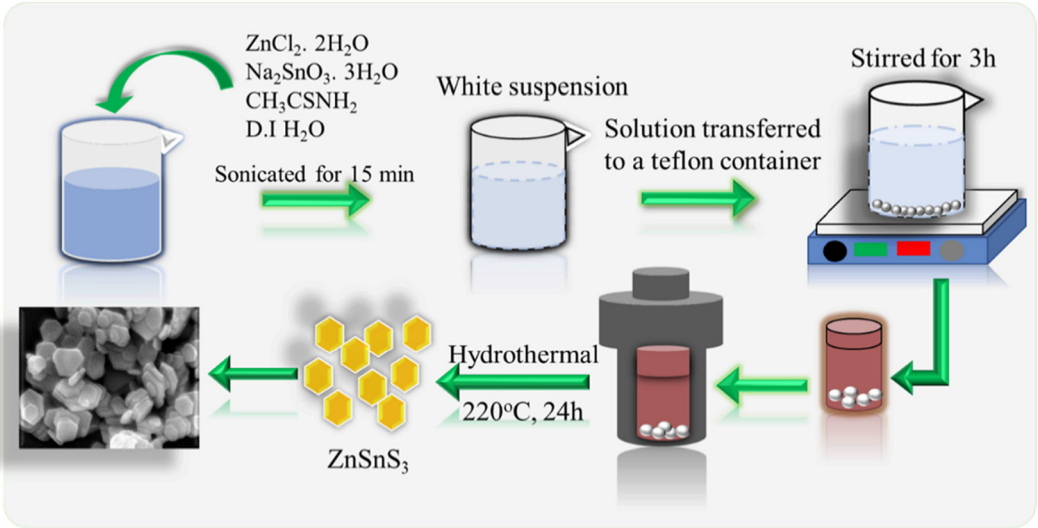

Scheme 1 Synthesis process scheme for LN-$ZnSnS_3$ nanocrystals.

vis–NIR spectrophotometer. The morphology and structure were investigated using a field-emission scanning electron microscope (FE-SEM, JEOL JSM-6700F) and a transmission electron microscope (TEM, JEOL JEM-2100F).

PFM and KPFM measurement

PFM was conducted with an Asylum Research MFP-3D atomic force microscopy (AFM) instrument at room temperature (rt) with a Ti/Ir (5/20) coated cantilever (ASYELEC-01, nominal spring constant 2 N m^{-1}, resonance frequency 81 kHz). PFM topography, amplitude and phase images were investigated at an applied bias voltage of ±7 V. For PFM, a ~200 nm thick film sample was deposited on the Si wafer substrate by drop casting from an aqueous dispersion. For Kelvin probe force microscopy (KPFM) measurement, a 2.5 V AC drive voltage, drive amplitude of 53 mV, and phase offset of 47° were applied at a resonance frequency of 81 kHz within a band range of 5 kHz in contact mode. The applied bias removes the external surface charges of the contact region area during scanning.

Results and discussion

Structure and optical properties

Fig. 1a represents the powder XRD signal of the as-synthesized ZTS NCs after 24 h, with the sharp and distinct peaks indicating good crystallinity, as shown in comparison to the simulated XRD pattern (DFT calculation using Mercury software). The XRD pattern of the LN-ZTS NCs is a good match to the simulated one, which indicates the successful formation of the rhombohedral phase (space group: *R3c*, 161) of ZTS NCs,[35] along with some minor extra peaks, corresponding to the cubic phase (JCPDS 28-1486) of ZTS (closed diamond).[44] The major diffraction peaks observed at 2θ = 26.4, 28.1, 32.2, 34.3, 39.0, 42.7, 49.9, 51.4, 54.4, 56.4, 58, 61.3, 65.1, and 71.5°, correspond to the (211), (1–10), (210), (200), (220), (321), (2–1–1), (320), (422), (433), (2–20), (330), (1–3–2), and (532) planes of rhombohedral LN-ZTS. However, it should be noted that a few peaks are common to both rhombohedral and cubic phases, namely at 2θ = 26.4, 34.3, 51.4, 54.4, 61.3, and 65.1°, and hence minor phase impurities cannot be ruled out in the first instance. The crystallite size calculated using the Scherrer equation[45] is about 10 nm. Moreover, an additional peak at 47.6° (open diamond) occurs due to the crystal plane corresponding to the inner Zn–S bond (JCPDS No. 05-0566).[46] A comparative analysis of the XRD results for the products at 6 h, 12 h, and 24 h, presented in Fig. S1a,† indicates that the LN-type rhombohedral phase becomes the predominant phase after 24 h. Fig. 1b shows the UV–VIS–NIR reflectance spectrum of LN-ZTS NCs, and a calculated indirect band gap of 1.95 eV is obtained for ZTS NCs using the Kubelka–Munk equation:[47] $[F(R)\cdot h\nu]^n = A(h\nu - E_g)$, where $F(R) = (1-R)^2/2R$, R is the reflectance, $h\nu$ = the energy of a photon, and n = 2 for a direct band gap and $\frac{1}{2}$ for an indirect band gap.

Chemical composition and morphology

X-ray photoelectron spectroscopy (XPS) confirms the chemical composition of LN-ZTS NCs. The survey spectrum (Fig. 1c) shows the presence of zinc, tin, and sulfur along with carbon and oxygen, which may arise from the hydrated precursor salt and water used in the reaction. For further analysis of the oxidation state of different ions, high-resolution spectra were also obtained for individual ions, as shown in Fig. 1(d–f). From the high-resolution spectrum of Zn (Fig. 1d) two major peaks at 1022.2 and 1045.2 eV are obtained, corresponding to Zn $2p_{3/2}$ and Zn $2p_{5/2}$, respectively, and confirming Zn^{2+} in ZTS NCs.[21] Sn states are shown in Fig. 1e, indicating the 3d state of Sn, which is further divided into two separate peaks, Sn $3d_{5/2}$ and Sn $3d_{3/2}$, due to spin–orbit interaction. The peak positions at

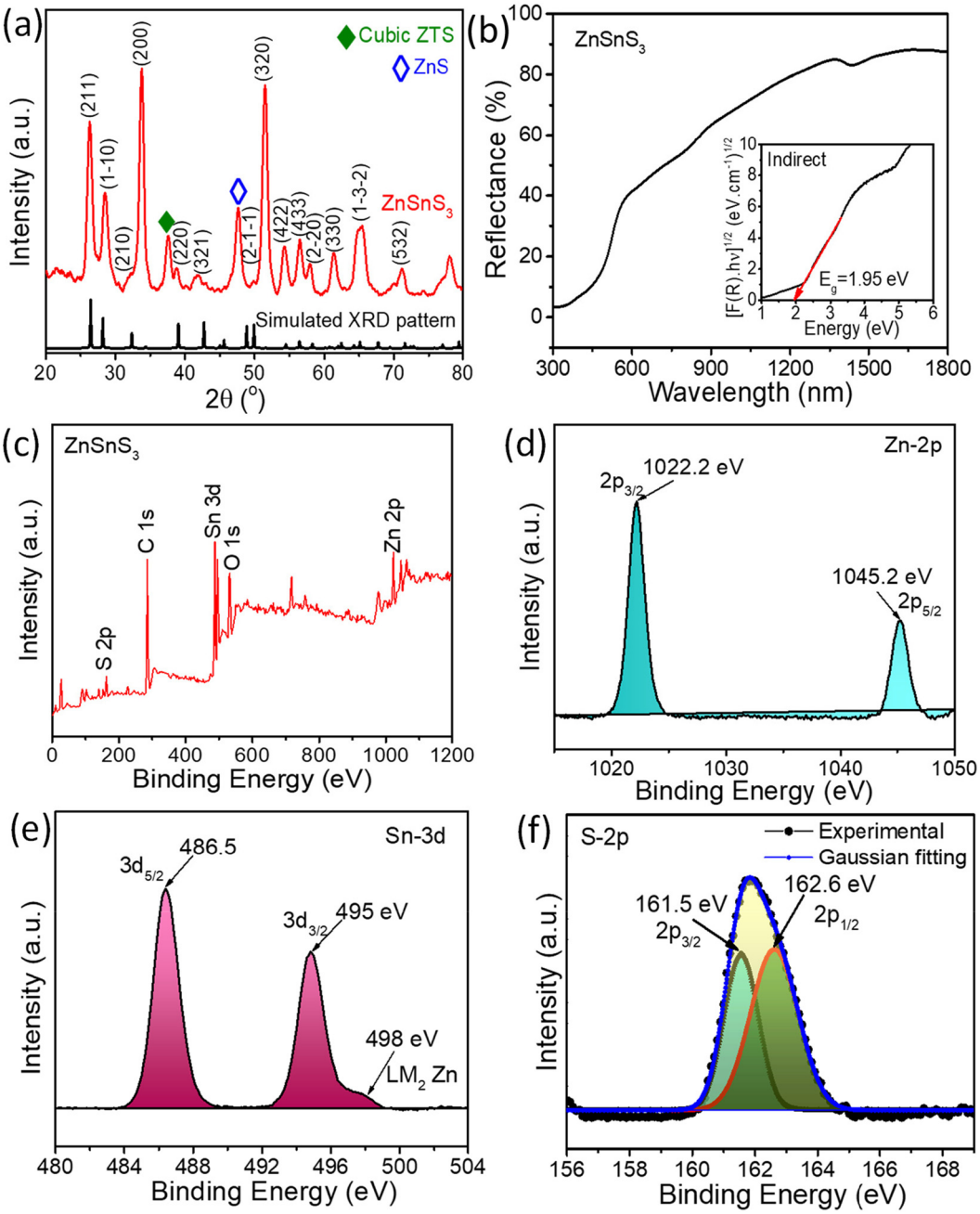

Fig. 1 (a) PXRD pattern of the as-synthesized rhombohedral LN-type $ZnSnS_3$. The bottom line indicates the simulated XRD pattern of rhombohedral $ZnSnS_3$ using the parameters in ref. 35. (b) Diffuse reflectance spectroscopy of $ZnSnS_3$, and the corresponding band gap calculated with the Kubelka–Munk equation (inset image). XPS spectra of as-synthesized $ZnSnS_3$ nanocrystals, (c) survey spectrum, high-resolution spectra of (d) Zn 2p state, (e) Sn-3d state, and (f) S-2p state.

486.5 and 495.0 eV are assigned to the $3d_{5/2}$ and $3d_{3/2}$ states of Sn with an energy separation of 8.5 eV, which indicates the presence of the +4 oxidation state of Sn.[48] In addition, after deconvolution of the S 2p spectrum (Fig. 1f) two discrete peaks with binding energies 161.5 and 162.6 eV are obtained and are attributed to S $2p_{3/2}$ and S $2p_{1/2}$, which may arise from the inner Sn–S and Zn–S bonds, respectively, further confirming the S^{2-} oxidation state of sulfur.[48]

The FE-SEM images (Fig. 2a) clearly show the uniform and homogeneous growth of ZTS NCs after 24 h with well-formed hexagonal flake-like morphology of an average diameter of 20–30 nm (longest length). Distinctly hexagonal ZTS can be confirmed from the TEM images (Fig. 2b). The HR-TEM image (Fig. 2c) of individual hexagonal nanoflake shows good crystallinity with distinct and continuous lattice fringes revealing an interplanar distance of ~0.35 nm, which corresponds to the

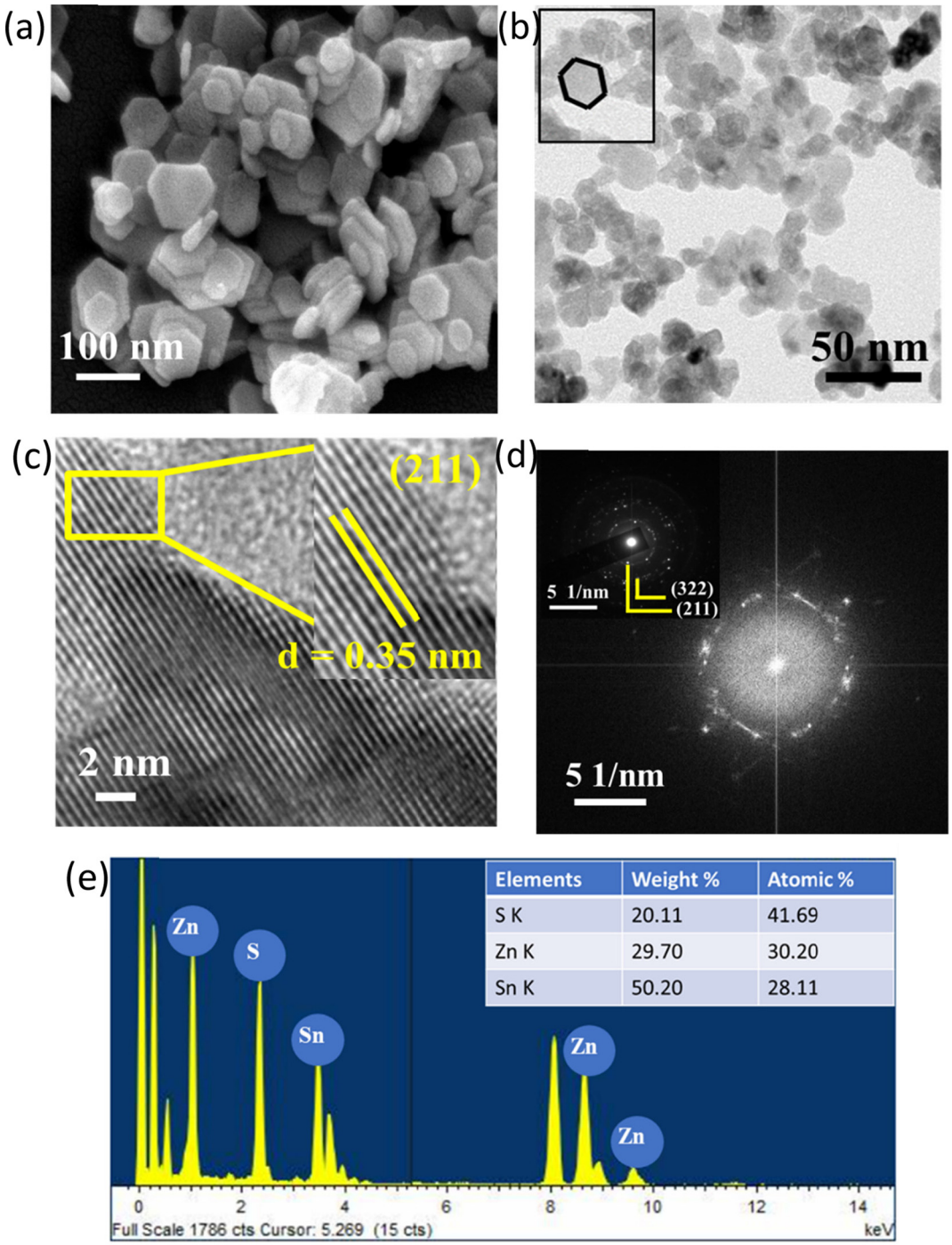

Fig. 2 (a) FE-SEM image, (b) low-resolution TEM image, (c) HR-TEM image and the interplanar spacing corresponding to the (211) plane (inset), (d) FFT and SAED pattern (inset), (e) energy dispersive X-ray spectrum and spectroscopic analysis (EDX) for ZTS NCs.

(211) lattice planes of the rhombohedral phase of the as-prepared LN-ZTS NCs. From the fast Fourier transformation (FFT) and selected area electron diffraction (SAED) pattern (inset) shown in Fig. 2d, prominent single crystalline diffraction rings are observed with distinct hexagonal symmetry from a single nanoplatelet. The EDS shown in Fig. 2e confirmed that the ratio of Zn, Sn and S is nearly stoichiometric. While the 24 h reaction product for the optimised LN-ZTS phase shows hexagonal morphology, broadly indicative of the R3c crystal structure, the more phase-impure 6 h and 12 h products morphologically show much smaller and less developed shapes of hexagonal nanoflakes (Fig. S1(b–e)†), further proving that the LN crystal structure might not be predominantly formed due to partial completion of the reaction.

Local piezoelectricity studies by PFM and KPFM

After confirming the structural and chemical purity of the desired LN-ZTS nanoflakes, the microscopic piezoelectric properties were investigated using PFM and KPFM. In order to understand the pure piezoelectric effect from the various noises that contribute to the electromagnetic (EM) response, the PFM phase change and also the shape of the hysteresis loops are crucial. The AFM topography, PFM amplitude and phase images at rt are shown in Fig. 3. The amplitude values are verified by calibrating the resonant frequency at 81 kHz on several regions of the same sample and also on different samples. The calibration exercise eliminates the Vegard strain effect in PFM, which is also essential to separate erroneous EM signals. The vertical (out-of-plane) PFM image (Fig. 3a) under no bias revealed no direct link between the microstructure and domain orientation, confirming that piezoelectric deformation dominates the PFM signals. The colour-changing images from yellow to reddish brown show the domain-switching phenomenon with the change in the polarity of the applied voltage at ±7 V (Fig. 3b and c) with no clear visible domain boundaries. However, the phase hysteresis loop (Fig. 3d) recorded from the areas showed a nearly 180° phase shift, *i.e.* fully switched piezoelectric domains, and good loop opening with the polarity change of the offset voltage. Fig. 3(e–g) show the corresponding amplitude images. From the slope of the butterfly loop (Fig. 3h), an effective d_{33} is estimated, which is crucial for assessing the efficiency and performance of piezoelectric materials.[49] The average calculated value of d_{33} is 19 ± 2 pm V^{-1}, which is higher than or comparable to that reported for lead-free perovskite nanomaterials.[50,51] The asymmetries observed between the positive and negative halves of the butterfly loop (Fig. 3h) suggest the existence of non-homogeneous piezo-domain boundaries, which may arise from the non-oriented nanoflakes and

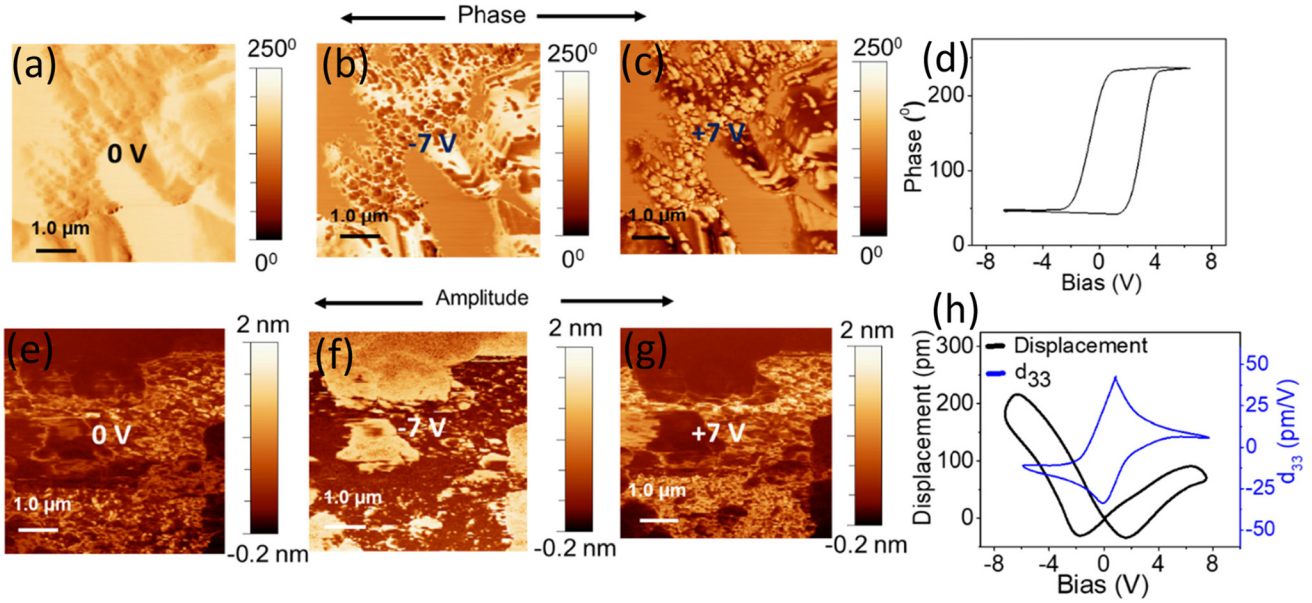

Fig. 3 PFM (a)–(c) phase images with a change of bias voltage ±7 V of the LN-ZTS NC film. (d) Plot of the phase change of the LN-ZTS NC film. (e)–(g) Amplitude images with the same change in bias voltage. (h) Butterfly loop and d_{33} plot.

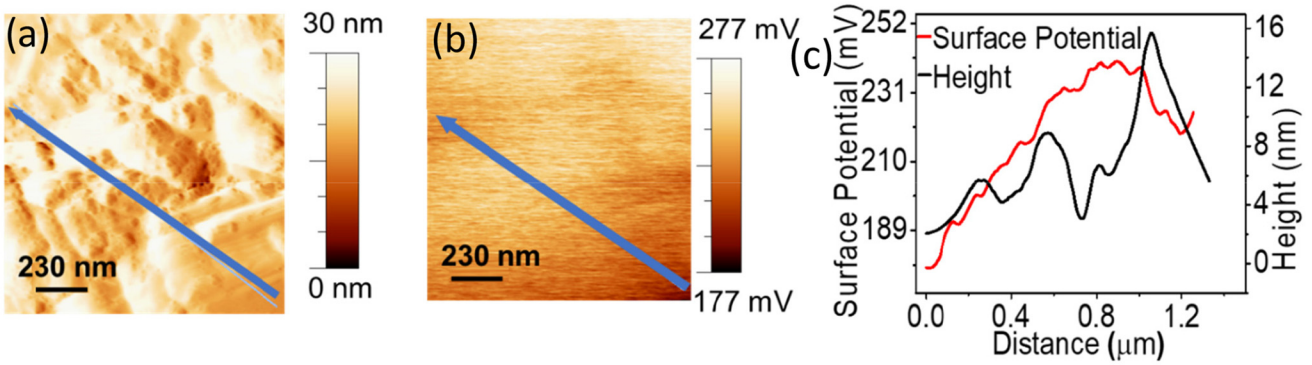

Fig. 4 (a) KPFM topography, (b) surface potential, and (c) their graphical variation in the LN-ZTS NC film along the line (as drawn).

domains in the deposited nanostructured film.[52–54] The hysteresis butterfly loop and phase hysteresis of the LN-ZTS NC film measured at the different regions of the sample and on different samples clearly indicate local polarization switching at the micro/nano scale (see Fig. S2†). We also performed KPFM measurements to explore the surface barrier potential on the LN-ZTS NCs, in a non-invasive way. The KPFM topography, surface potential mapping and corresponding line profile are shown in Fig. 4(a and b). A surface charge potential difference of 65 mV was observed (Fig. 4c) from the LN-ZTS film, which suggests a strong surface potential value on a par with other lead-free piezoelectric materials.[55–58] The nanoscale domain features in LN-ZTS NCs are in strong agreement with previous theoretical understanding, and the experimental validation presented here indicates potentially valuable ferroelectric/piezoelectric properties in the LN-type rhombohedral phase as well as plausible emergent photonic characteristics.[35] A detailed domain dynamics study from a single nanoflake may reveal domain migration behaviour and provides scope for further study in this system.

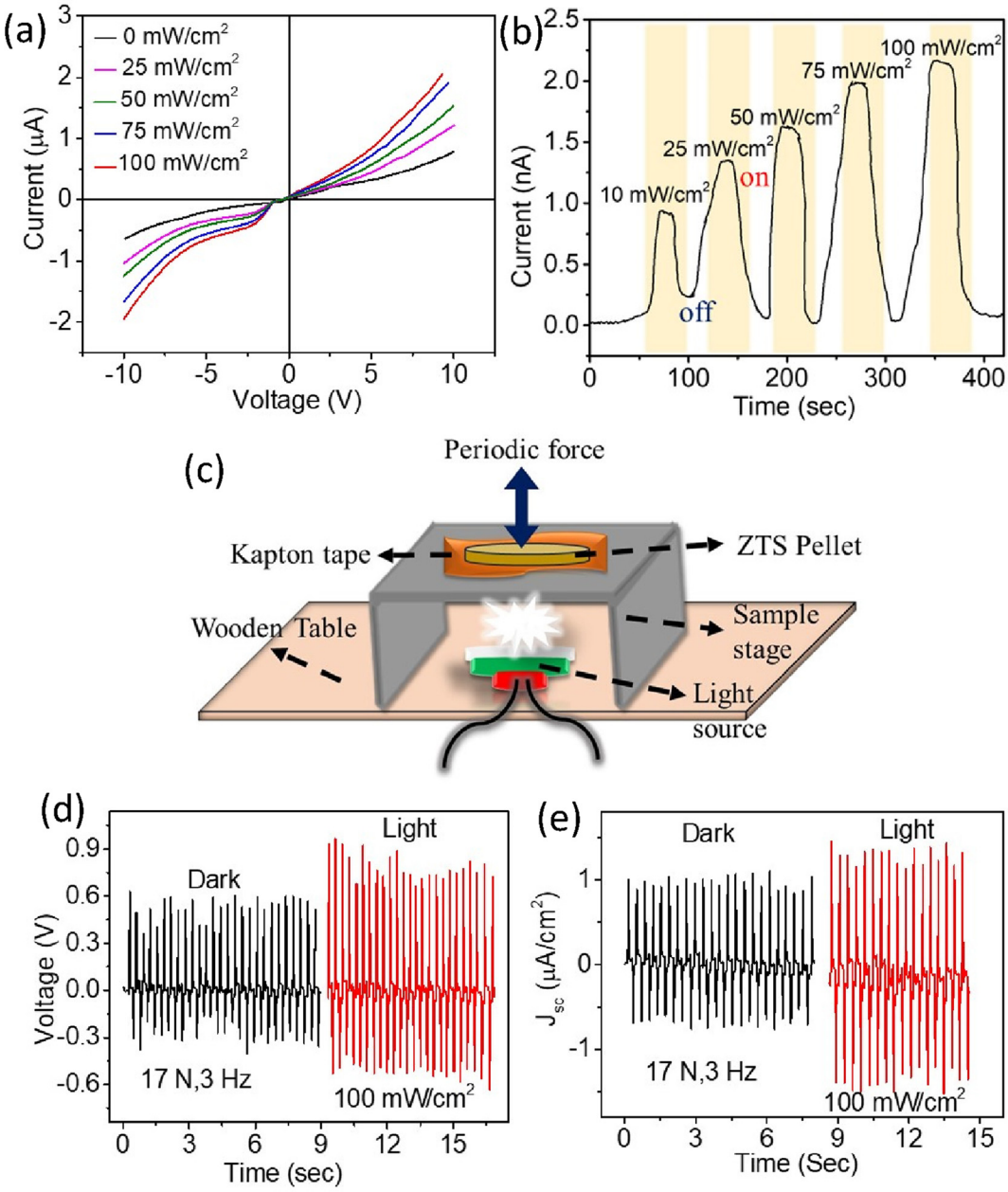

Fig. 5 (a) Current *vs.* voltage (*I*–*V*) curves measured in the dark (black) and under light with different intensities at an applied bias of ±10 V, (b) time-dependent light on–off response under various light intensities under zero-bias conditions, (c) schematic diagram of custom-built piezophototronic measurement setup in our laboratory, (d and e) variation in voltage and current density under dark and light (100 mW cm^{-2}) conditions for ZTS NCs pellet at 17 N and 3 Hz.

Optoelectronic properties

While the piezoelectric properties are agreed, the fundamental optoelectronic properties were investigated from the current–voltage (*I–V*) measurements of LN-ZTS NCs under dark and variable intensities of white-light-illuminated conditions (Fig. 5a). Importantly, the *I–V* measurement displays asymmetric nonlinear characteristics, revealing Schottky-type behaviour at the metal semiconductor Au/LN-ZTS junction due to back-to-back Schottky barriers.[59] As predicted, a strong photoresponse under illumination may be observed from Fig. 5a. While a significant dark current of 0.6 μA was recorded at an applied bias of 10 V, possibly generated from leakage, the current was enhanced considerably to 2.1 μA under white light illumination at an intensity of 100 mW cm^{-2}. The data were recorded from several Schottky devices through repeated measurement across various seasons and times. Additionally, the photo-switching characteristics of the material were confirmed under zero-bias conditions, as shown in Fig. 5b, with an average decay rate of 0.1 nA s^{-1}.

Light-induced piezoelectric energy harvesting

The piezoelectric energy harvesting performance of the LN-ZTS nanogenerator device in the dark without light stimulation was recorded using a mechanical vibrational energy harvesting setup,[39,60] under modulated forces and frequencies ranging from 1 N to 17 N and 1 Hz to 5 Hz. To first confirm the piezoelectric effect of the LN-ZTS device, polarity checking under both forward and reverse conditions was performed under 17 N and 5 Hz. With reversal of the connection, the positive and negative peaks of V_{oc} and J_{sc} were also reversed, confirming the piezoelectric nature of the ZTS device, as illustrated in Fig. S3 (a and b†). The LN-ZTS piezoelectric nanogenerator without any light stimulation showed a linear increase in V_{oc} and J_{sc},[61] from 0.4 V to 0.7 V, and from 0.4 μA cm^{-2} to 1 μA cm^{-2}, respectively, with the force increasing from 1 N to 17 N at a constant frequency of 5 Hz (Fig. S4(a and b)†). Based on the increase in peak voltage V_p with the applied force, a mechano-sensitivity of ~20 mV N^{-1} was calculated from the slope of the graph presented in Fig. S4c.†[62] On the other hand, with the increase in frequency, V_{oc} and J_{sc} increased from 0.1 V to 0.7 V and from 0.2 μA cm^{-2} to 1 μA cm^{-2}, respectively, when the frequency rose from 1 Hz to 5 Hz at 17 N (Fig. S4(d and e)†). This increase in V_{oc} and J_{sc} with force may be directly related to piezo-charge generation within a short period, as reported earlier.[63] A performance parametric comparison with so far reported binary metal piezoelectric sulfides, shown in Table S1,† indicates comparable responses from LN-ZTS nanoflakes.

Finally, to explore the light-stimulated piezoelectric vibrational energy harvesting possibility from LN-ZTS NCs, a custom-built setup was used, as shown schematically in Fig. 5(c). The V_{oc} and J_{sc} values were measured with a force gauge (Lutron Force Gauge FG-20 KG), where force was applied to the back of the device, both under both dark and illuminated conditions, as indicated in Fig. 5(d and e). At different force and frequency conditions up to 17 N and 3 Hz, V_{oc} and J_{sc} showed a significant increase in the presence of light. J_{sc}

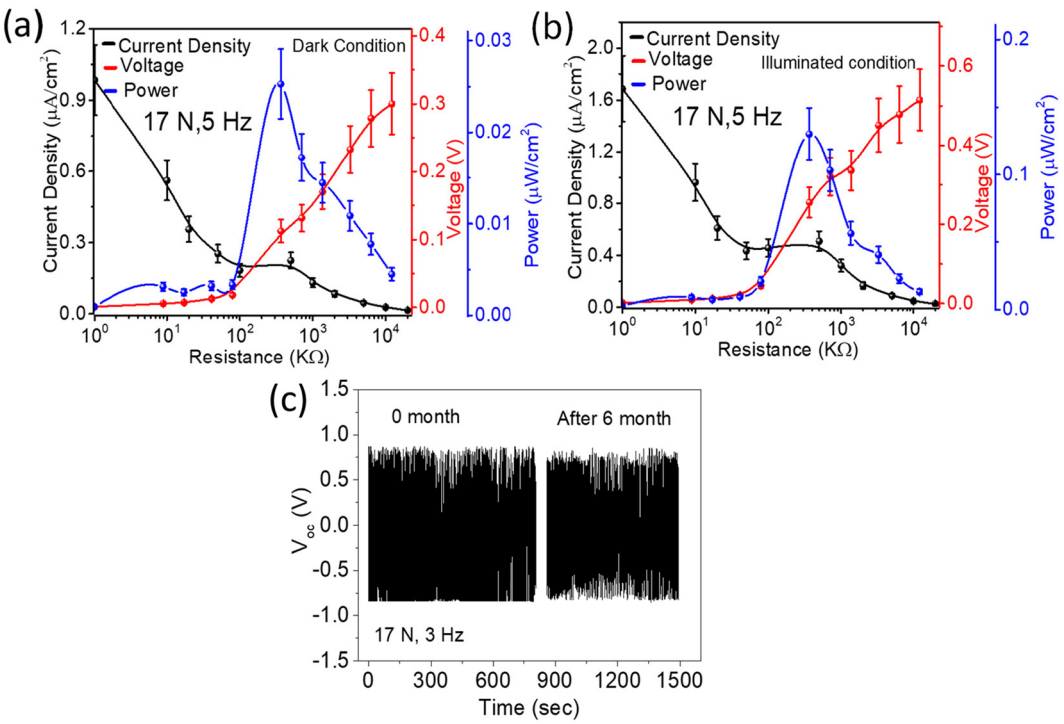

Fig. 6 Variation of *J*, *V*, and *P* output with load resistance in (a) dark conditions, (b) light-illuminated conditions. (c) Fatigue test over 20 000 cycles and after 6 months at 17 N and 5 Hz.

increased from 0.9 μA cm^{-2} in the dark to 1.3 μA cm^{-2}, representing a nearly 44% rise, and V_{oc} increased from 0.5 V to 0.8 V, *i.e.* about a 60% increase, when illuminated with a light of intensity of 100 mW cm^{-2} while the mechanical force was applied consistently (Fig. S5†). Under an applied mechanical force, both current and voltage increase due to the synergistic effect of strain-induced piezoelectric polarization and enhanced photon absorption. Provided a junction geometry is used, this effect might be well applied for photovoltaic applications, by improving charge separation and lowering recombination losses, which will be the subject of future study. We therefore show that the coupling mechanism plays a crucial role in modulating carrier transport and dipole dynamics.[64–73] The output voltage, current and power were therefore recorded from the nanogenerator with an external resistance load under the optimised 17 N and 3 Hz. A maximum output power of 0.025 μW cm^{-2} from the device under dark conditions (Fig. 6a) and an output power of 0.13 μW cm^{-2} with a light intensity of 100 mW cm^{-2} (Fig. 6b) can be viably extracted. Moreover, The LN-ZTS piezo-nanogenerator under illumination can endure nearly 20 000 cycles during 1 h of continuous operation, and even after 6 months can provide stable output power with only a minor decrease (~5%), as indicated in Fig. 6(c). The stability and durability of the LN-ZTS piezophototronic responses suggest that, with further optimization of the device geometry and density and by controlling the morphology and orientation of the LN-ZTS NCs in the generator devices, higher performance might reasonably be achieved. When compared to very few sulfide-based piezoephototronic nanomaterials reports available (see Table S2†), LN-ZTS NCs with a high d_{33} value and an already low band gap, will have abundant potential in the near future to be studied as feasible economic candidates for a multitude of energy harvesting applications. To the best of our knowledge, there has been no prior report on piezopotential-induced energy harvesting using ternary metal sulfide nanostructures, and this finding opens up new possibilities for identifying new photoresponsive piezoelectric ternary sulfide semiconductors.

Conclusions

With the augmented hunt for eco-friendly, lead-free, multifunctional, self-powered electronics materials, the focus is now mainly on coupling photonic and both ferroelectric and piezoelectric properties. Towards that end, ternary chalcogenide compounds have rarely been explored. Recent theoretical and specific experimental reports on $LiNbO_3$-structured $ZnSnS_3$ as a candidate semiconducting ferroelectric material, open up possibilities for investigating both mechanical and light energy harvesting using a ternary sulfide-based material. Herein, we propose a one-step hydrothermal synthesis of hexagonal R3c, $LiNbO_3$ type-$ZnSnS_3$ (LN-ZTS) nanoflakes of dimension 20–30 nm and show that with a band gap energy of ~1.9 eV and possessing a piezoelectric coefficient (d_{33}) of ~19 pm V^{-1}, the LN-ZTS nanogenerator can harvest an output power of ~0.13 μW cm^{-2} for 100 mW cm^{-2} under a constant mechanical impact. While the output power is still not on a par with oxide-based ceramic piezophototronic systems, identifying a functional sulfide material using a low-cost synthesis method is set to offer a sustainable direction for photoresponsive vibrational energy harvesting.

Author contributions

SD and SP have contributed equally. SD carried out the materials synthesis, characterizations and device fabrication. SP carried out piezoelectric and piezophototronics measurements. AD conceptualized the project, received external funding, and supervised the entire work. All authors contributed to the data discussion and analysis, and final manuscript writing.

Data availability

The data supporting this article have been included as part of the ESI.†

Conflicts of interest

The authors declare no competing financial or ethical interest.

Acknowledgements

S. D. thanks CSIR-India (09/0080(11533)/2021-EMR-I) for the research fellowship. S. P. thanks IACS for research fellowship. A. D. acknowledges DST funded Technical Research Center (TRC), IACS for financial support.

References

1 B. Dai, G. M. Biesold, M. Zhang, H. Zou, Y. Ding, Z. L. Wang and Z. Lin, *Chem. Soc. Rev.*, 2021, **50**, 13646–13691.
2 Y. Zhang, H. Kim, Q. Wang, W. Jo, A. I. Kingon, S.-H. Kim and C. K. Jeong, *Nanoscale Adv.*, 2020, **2**, 3131–3149.
3 H. Wei, H. Wang, Y. Xia, D. Cui, Y. Shi, M. Dong, C. Liu, T. Ding, J. Zhang, Y. Ma, N. Wang, Z. Wang, Y. Sun, R. Wei and Z. Guo, *J. Mater. Chem. C*, 2018, **6**, 12446–12467.
4 Z. L. Wang, X. Y. Kong, Y. Ding, P. Gao, W. L. Hughes, R. Yang and Y. Zhang, *Adv. Funct. Mater.*, 2004, **14**, 943–956.
5 H. D. Espinosa, R. A. Bernal and M. Minary-Jolandan, *Adv. Mater.*, 2012, **24**, 4656–4675.
6 J. Zhang, C. Wang and C. Bowen, *Nanoscale*, 2014, **6**, 13314–13327.
7 M. Yang and P. Sheng, *Annu. Rev. Mater. Res.*, 2017, **47**, 83–114.

8 X. Lv, T. Zheng, C. Zhao, J. Yin, H. Wu and J. Wu, *Acc. Mater. Res.*, 2022, **3**, 461–471.
9 X. Lv, X. X. Zhang and J. Wu, *J. Mater. Chem. A*, 2020, **8**, 10026–10073.
10 J. Wu, D. Xiao and J. Zhu, *Chem. Rev.*, 2015, **115**, 2559–2595.
11 L. Pan, S. Sun, Y. Chen, P. Wang, J. Wang, X. Zhang, J. J. Zou and Z. L. Wang, *Adv. Energy Mater.*, 2020, **10**, 2000214.
12 Q. Yang, X. Guo, W. Wang, Y. Zhang, S. Xu, D. H. Lien and Z. L. Wang, *ACS Nano*, 2010, **4**, 6285–6291.
13 Q. Yang, W. Wang, S. Xu and Z. L. Wang, *Nano Lett.*, 2011, **11**, 4012–4017.
14 J. Sun, Q. Hua, R. Zhou, D. Li, W. Guo, X. Li, G. Hu, C. Shan, Q. Meng, L. Dong, C. Pan and Z. L. Wang, *ACS Nano*, 2019, **13**, 4507–4513.
15 Z. L. Wang, *Adv. Mater.*, 2012, **24**, 4632–4646.
16 C. Pan, J. Zhai and Z. L. Wang, *Chem. Rev.*, 2019, **119**, 9303–9359.
17 R. Chen, M. I. BaktiUtama, Z. Peng, B. Peng, Q. Xiong and H. Sun, *Adv. Mater.*, 2011, **23**, 1404–1408.
18 F. Zhang, Y. Ding, Y. Zhang, X. Zhang and Z. L. Wang, *ACS Nano*, 2012, **6**, 9229–9236.
19 L. Zhu and Z. L. Wang, *Adv. Funct. Mater.*, 2019, **29**, 1808214.
20 F. Mushtaq, X. Chen, M. Hoop, H. Torlakcik, E. Pellicer, J. Sort, C. Gattinoni, B. J. Nelson and S. Pané, *iScience*, 2018, **4**, 236–246.
21 S. Barman and A. Datta, *Mater. Chem. Phys.*, 2022, **290**, 126507.
22 H. T. Yi, T. Choi, S. G. Choi, Y. S. Oh and S. W. Cheong, *Adv. Mater.*, 2011, **23**, 3403–3407.
23 H. Han, D. Kim, S. Chae, J. Park, S. Y. Nam, M. Choi, K. Yong, H. J. Kim, J. Son and H. M. Jang, *Nanoscale*, 2018, **10**, 13261–13269.
24 Y. Saito, H. Takao, T. Tani, T. Nonoyama, K. Takatori, T. Homma, T. Nagaya and M. Nakamura, *Nature*, 2004, **432**, 81–84.
25 F. Li, D. Lin, Z. Chen, Z. Cheng, J. Wang, C. Li, Z. Xu, Q. Huang, X. Liao, L. Q. Chen, T. R. Shrout and S. Zhang, *Nat. Mater.*, 2018, **17**, 349–354.
26 M. T. Chorsi, T. T. Le, F. Lin, T. Vinikoor, R. Das, J. F. Stevens, C. Mundrane, J. Park, K. T. M. Tran, Y. Liu, J. Pfund, R. Thompson, W. He, M. Jain, M. D. Morales-Acosta, O. R. Bilal, K. Kazerounian, H. Ilies and T. D. Nguyen, *Sci. Adv.*, 2023, **9**, eadg6075.
27 C. Xu, Y. Song, M. Han and H. Zhang, *Microsyst. Nanoeng.*, 2021, **7**, 25.
28 G. Zhao, X. Zhang, X. Cui, S. Wang, Z. Liu, L. Deng, A. Qi, X. Qiao, L. Li, C. Pan, Y. Zhang and L. Li, *ACS Appl. Mater. Interfaces*, 2018, **10**, 15855–15863.
29 N. Sezer and M. Koç, *Nano Energy*, 2021, **80**, 105567.
30 N. Jia, T. Wang, J. Duan, K. Qiang, S. Xia, H. Du, F. Li and Z. Xu, *ACS Appl. Mater. Interfaces*, 2022, **14**, 8137–8145.
31 Y. Fu, Z. Ren, L. Guo, X. Li, Y. Li, W. Liu, P. Li, J. Wu and J. Ma, *J. Mater. Chem. C*, 2021, **9**, 12596–12604.
32 G. T. Hwang, M. Byun, C. K. Jeong and K. J. Lee, *Adv. Healthcare Mater.*, 2015, **4**, 646–658.
33 A. Zaszczyńska, A. Gradys and P. Sajkiewicz, *Polymers*, 2020, **12**, 2754.
34 H. Xu, C. Wang, J. F. Zhang, J. Zhang, L. Cao, B. Zhang and X. Ou, *ACS Sustainable Chem. Eng.*, 2020, **8**, 4464–4473.
35 B. Kolb and A. M. Kolpak, *Chem. Mater.*, 2015, **27**, 5899–5906.
36 R. A. Jishi and M. A. Lucas, *Int. J. Photoenergy*, 2016, **9**, 6193502.
37 A. Datta, D. Mukherjee, C. Kons, S. Witanachchi and P. Mukherjee, *Small*, 2014, **10**, 4093–4099.
38 D. Mukherjee, A. Datta, C. Kons, M. Hordagoda, S. Witanachchi and P. Mukherjee, *Appl. Phys. Lett.*, 2014, **105**, 212903.
39 S. Barman, S. Paul, P. Ranjan, S. Das and A. Datta, *J. Mater. Sci.*, 2023, **58**, 7060–7075.
40 S. Barman, S. Paul and A. Datta, *Interdisciplinary Research in Technology and Management (IRTM)*, Kolkata, India, 2022, pp. 1–4.
41 S. Paul, S. Barman and A. Datta, *J. Mater. Sci.*, 2024, **59**, 17968–17990.
42 H. Jia, M. Dirican, N. Sun, C. Chen, C. Yan, P. Zhu, X. Dong, Z. Du, H. Cheng, J. Guo and X. Zhang, *ChemElectroChem*, 2019, **6**, 1183–1191.
43 R. Ding, Y. Lyu, Z. Wu, F. Guo, W. F. Io, S. Y. Pang, Y. Zhao, J. Mao, M. C. Wong and J. Hao, *Adv. Mater.*, 2021, **33**, 2101263.
44 X. Liu, Y. Hao, J. Shu, H. M. K. Sari, L. Lin, H. Kou, J. Li, W. Liu, B. Yan, D. Li, J. Zhang and X. Li, *Nano Energy*, 2019, **57**, 414–423.
45 K. He, N. Chen, C. Wang, L. Wei and J. Chen, *Cryst. Res. Technol.*, 2018, **53**, 1700157.
46 M. Mao, L. Jiang, L. Wu, M. Zhang and T. Wang, *J. Mater. Chem. A*, 2015, **3**, 13384–13389.
47 S. Lacombe, H. Cardy, N. Soggiu, S. Blanc, J. L. Habib-Jiwan and J. P. Soumillion, *Microporous Mesoporous Mater.*, 2001, **46**, 311–325.
48 S. Das, B. P. Mondal, P. Ranjan and A. Datta, *ACS Appl. Mater. Interfaces*, 2023, **15**, 56022–56033.
49 J. S. Sekhon, L. Aggarwal and G. Sheet, *Appl. Phys. Lett.*, 2014, **104**, 162908.
50 A. Rovisco, A. Dos Santos, T. Cramer, J. Martins, R. Branquinho, H. Águas, B. Fraboni, E. Fortunato, R. Martins, R. Igreja and P. Barquinha, *ACS Appl. Mater. Interfaces*, 2020, **12**, 18421–18430.
51 K. P. Kelley, D. E. Yilmaz, L. Collins, Y. Sharma, H. N. Lee, D. Akbarian, A. C. T. Van Duin, P. Ganesh and R. K. Vasudevan, *Phys. Rev. Mater.*, 2020, **4**, 024407.
52 J. Jiang, Y. Bitla, C.-W. Huang, T.-H. Do, H.-J. Liu, Y.-H. Hsieh, C.-H. Ma, C.-Y. Jang, Y.-H. Lai, P.-W. Chiu, W.-W. Wu, Y.-C. Chen, Y.-C. Zhou and Y.-H. Chu, *Sci. Adv.*, 2017, **3**, e1700121.
53 F. Xue, J. Cao, X. Li, J. Feng, M. Tao and B. Xue, *J. Mater. Chem. C*, 2021, **9**, 7568–7574.

54 J. Liu, Q. Zhao, Y. Dong, X. Sun, Z. Hu, H. Dong, W. Hu and S. Yan, *ACS Appl. Mater. Interfaces*, 2020, **12**, 29818–29825.
55 J. Döring, L. M. Eng and S. C. Kehr, *J. Appl. Phys.*, 2016, **120**, 084103.
56 L. Lechaptois, Y. Prado and O. Pluchery, *Nanoscale*, 2023, **15**, 7510–7516.
57 Q. Li, X. Li, M. Zheng, F. Luo, L. Zhang, B. Zhang and B. Jiang, *Adv. Funct. Mater.*, 2024, 2417279.
58 L. Zhou, Q. Fang, M. Liu, S. Farhan, S. Yang and Y. Wu, *Inorg. Chem.*, 2024, **63**(44), 21202–21211.
59 A. Di Bartolomeo, A. Grillo, F. Urban, L. Iemmo, F. Giubileo, G. Luongo, G. Amato, L. Croin, L. Sun, S. J. Liang and L. K. Ang, *Adv. Funct. Mater.*, 2018, **28**, 1800657.
60 S. Paul, S. Barman, A. Pal, A. Mukherjee, S. Ghosh and A. Datta, *Chem. Mater.*, 2023, **35**(16), 6463–6471.
61 T. M. Guo, Y. J. Gong, Z. G. Li, Y. M. Liu, W. Li, Z. Y. Li and X. H. Bu, *Small*, 2022, **18**, 2103829.
62 E. S. Hosseini, L. Manjakkal, D. Shakthivel and R. Dahiya, *ACS Appl. Mater. Interfaces*, 2020, **12**, 9008–9016.
63 A. Datta, Y. S. Choi, E. Chalmers, C. Ou and S. Kar-Narayan, *Adv. Funct. Mater.*, 2017, **27**, 1604262.
64 R. Yang, Y. Qin, L. Dai and Z. L. Wang, *Nat. Nanotechnol.*, 2009, **4**, 34–39.
65 S. Jeong, M. W. Kim, Y. R. Jo, T. Y. Kim, Y. C. Leem, S. W. Kim, B. J. Kim and S. J. Park, *ACS Appl. Mater. Interfaces*, 2018, **10**, 28736–28744.
66 X. Zhang, Y. Qiu, D. Yang, B. Li, H. Zhang and L. Hu, *RSC Adv.*, 2018, **8**, 15290–15296.
67 S. Lu, J. Qi, S. Liu, Z. Zhang, Z. Wang, P. Lin, Q. Liao, Q. Liang and Y. Zhang, *ACS Appl. Mater. Interfaces*, 2014, **6**, 14116–14122.
68 F. Zhang, S. Niu, W. Guo, G. Zhu, Y. Liu, X. Zhang and Z. L. Wang, *ACS Nano*, 2013, **7**, 4537–4544.
69 S. C. Rai, K. Wang, Y. Ding, J. K. Marmon, M. Bhatt, Y. Zhang, W. Zhou and Z. L. Wang, *ACS Nano*, 2015, **9**, 6419–6427.
70 C. Du, W. Hu and Z. L. Wang, *Adv. Eng. Mater.*, 2018, **20**, 1700760.
71 M. Peng, Y. Liu, A. Yu, Y. Zhang, C. Liu, J. Liu, W. Wu, K. Zhang, X. Shi, J. Kou, J. Zhai and Z. L. Wang, *ACS Nano*, 2016, **10**, 1572–1579.
72 Y. Y. Tang, Y. L. Zeng and R. G. Xiong, *J. Am. Chem. Soc.*, 2022, **144**, 8633–8640.
73 H. Li, Y. Sang, S. Chang, X. Huang, Y. Zhang, R. Yang, H. Jiang, H. Liu and Z. L. Wang, *Nano Lett.*, 2015, **15**, 2372–2379.